Monthly Notices
of the
ROYAL ASTRONOMICAL SOCIETY

MNRAS **520,** 2952–2964 (2023) https://doi.org/10.1093/mnras/stad338
Advance Access publication 2023 January 31

Formation of polar circumstellar discs in binary star systems

Jeremy L. Smallwood ,[1,2]⋆ Rebecca G. Martin [2] and Stephen H. Lubow [3]

[1] *Institute of Astronomy and Astrophysics, Academia Sinica, Taipei 10617, Taiwan*
[2] *Department of Physics and Astronomy, University of Nevada, Las Vegas, 4505 South Maryland Parkway, Las Vegas, NV 89154, USA*
[3] *Space Telescope Science Institute, Baltimore, MD 21218, USA*

Accepted 2023 January 23. Received 2023 January 21; in original form 2022 July 28

ABSTRACT

We investigate the flow of material from highly misaligned and polar circumbinary discs that feed the formation of circumstellar discs around each binary component. With 3D hydrodynamic simulations we consider equal mass binaries with low eccentricity. We also simulate inclined test particles and highly misaligned circumstellar discs around one binary component for comparison. During Kozai–Lidov (KL) cycles, the circumstellar disc structure is altered through exchanges of disc eccentricity with disc tilt. Highly inclined circumstellar discs and test particles around individual binary components can experience very strong KL oscillations. The continuous accretion of highly misaligned material from the circumbinary disc allows the KL oscillations of circumstellar discs to be long-lived. In this process, the circumbinary material is continuously delivered with a high inclination to the lower inclination circumstellar discs. We find that the simulation resolution is important for modelling the longevity of the KL oscillations. An initially polar circumbinary disc forms nearly polar, circumstellar discs that undergo KL cycles. The gas steams accreting onto the polar circumstellar discs vary in tilt during each binary orbital period, which determines how much material is accreted onto the discs. The long-lived KL cycles in polar circumstellar discs may lead to the formation of polar *S*-type planets in binary star systems.

Key words: accretion, accretion discs – binaries: general – circumstellar matter.

1 INTRODUCTION

The majority of stars born in dense stellar clusters are part of binary star systems (Duquennoy & Mayor 1991; Ghez, Neugebauer & Matthews 1993; Duchêne & Kraus 2013). The observed orbital eccentricities of binaries vary with orbital separation (Raghavan et al. 2010; Tokovinin & Kiyaeva 2016). For tight binaries, the eccentricities are small, which implies that there has been circularization of the binary orbit caused by stellar tidal dissipation (Zahn 1977). More widely separated binaries have observed eccentricities ranging from $e_{\rm b} = 0.39$ to 0.59, with a considerable number of highly eccentric systems with $e_{\rm b} > 0.8$. The interactions of the binary with surrounding gas may be responsible for the present-day observed binary eccentricities (Goldreich & Tremaine 1980; Artymowicz et al. 1991; Artymowicz 1992; Armitage & Natarajan 2005; Cuadra et al. 2009; Roedig et al. 2011; Muñoz, Miranda & Lai 2019; Zrake et al. 2021). Circumbinary discs of gas and dust are sometimes observed to be responsible to be providing accreting material onto the binary (e.g. Alves et al. 2019). The gas flow dynamics from the circumbinary disc onto the binary components has significant implications for planet formation scenarios in binary systems.

Circumbinary discs are commonly observed to be moderately to highly misaligned to the binary orbital plane. For example, the pre-main sequence binary KH 15D has a circumbinary disc inclined by $5 - 16^{\circ}$ (Chiang & Murray-Clay 2004; Smallwood et al. 2019; Poon, Zanazzi & Zhu 2021). The radial extent of the disc is narrow and presumed to be rigidly precessing to explain the unique periodic light curve. A $\sim 60^{\circ}$ inclined circumbinary disc is found around the main-sequence binary IRS 43 (Brinch et al. 2016), along with misaligned circumstellar discs around each binary component. There is an observed misalignment of about 70° between the circumbinary disc and the circumprimary disc in HD 142527 (Marino, Perez & Casassus 2015; Owen & Lai 2017). Another young binary, HD 98800 BaBb, has the only observed polar (inclined by $\sim 90^{\circ}$) gaseous circumbinary disc (Kennedy et al. 2019). The 6–10 Gyr old binary system, 99 Herculis, has a nearly polar (about 87°) debris ring (Kennedy et al. 2012; Smallwood et al. 2020). Apart from binaries, stars may also form in higher-order systems (Tokovinin 2014a, b). The circumtriple disc around the hierarchical triple star system, GW Ori, is tilted by about 38° (Bi et al. 2020; Kraus et al. 2020; Smallwood et al. 2021a).

The observations of inclined circumbinary discs have implications on planet formation models. Observations from space and ground-based telescopes reveal that ∼50 per cent of the confirmed exoplanets reside in binary systems (Horch et al. 2014; Deacon et al. 2016; Ziegler et al. 2018). For example, the binary system γ Cep AB hosts a giant planet around the primary star, γ Cep Ab (Hatzes et al. 2003). It is crucial to study the structure and evolution of protoplanetary discs since these are the sites for planet formation (D'Angelo & Lissauer 2018). A forming planet's orbital properties are directly related to the orientation of the protoplanetary disc. For example, the observed young binary system XZ Tau shows both the circumprimary and circumsecondary discs are misaligned to the binary orbital plane (Ichikawa et al. 2021). The binary system HD 142527 shows the presence of a misaligned inner disc around one of the stellar components, presumably fed from the circumbinary disc

---

⋆ E-mail: jlsmallwood@asiaa.sinica.edu.tw

Published by Oxford University Press on behalf of Royal Astronomical Society

(Price et al. 2018b). Furthermore, IRAS 04158+2805 is a binary system where the two circumstellar discs and the circumbinary discs have been observed to be misaligned (Ragusa et al. 2021). Therefore, highly inclined circumstellar discs may give birth to planets on highly tilted orbits.

Due to viscous dissipation, a misaligned circumbinary disc undergoes nodal precession and evolves towards either a coplanar or polar alignment. For an initially low-inclination circumbinary disc, the disc precesses about the angular momentum vector of the binary and eventually evolves to be coplanar to the binary orbital plane (Facchini, Lodato & Price 2013; Foucart & Lai 2014). Slightly misaligned discs around an eccentric binary undergo tilt oscillations as they align, due to the non-axisymmetric potential produced by the eccentric binary (Smallwood et al. 2019, 2020). For highly inclined discs around eccentric orbit binaries, the angular momentum vector of the disc precesses about the eccentricity vector of the binary (e.g. Aly et al. 2015), which leads the disc to align perpendicular (i.e. polar) to the binary orbital plane (Martin & Lubow 2017; Lubow & Martin 2018; Zanazzi & Lai 2018; Martin & Lubow 2018; Cuello & Giuppone 2019). A massive circumbinary disc that is undergoing polar alignment aligns to a generalized polar state which is less than 90° (Zanazzi & Lai 2018; Martin & Lubow 2019; Chen et al. 2019).

Circumbinary gas discs contain a central cavity around the binary where little material is present. The cavity size is determined by where the tidal torque is balanced with the viscous torque (Artymowicz & Lubow 1994; Lubow, Martin & Nixon 2015; Miranda & Lai 2015; Franchini, Lubow & Martin 2019b; Hirsh et al. 2020; Ragusa et al. 2020). The strength of the binary torque on the disc is dependent on the tilt of the circumbinary disc and binary eccentricity. The tidal torque at a given radius is zero when the circumbinary disc is polar and the binary eccentricity approaches $e_{\rm b} = 1$ (Lubow & Martin 2018) or if the disc is retrograde (e.g. Nixon, King & Price 2013). In the simplest models, the production of an outward forcing torque by the binary can prevent circumbinary material from flowing through the cavity (Lynden-Bell & Pringle 1974; Pringle 1991). However, material from the circumbinary disc flows through the binary cavity in the form of gaseous streams (e.g. Artymowicz & Lubow 1996; Günther & Kley 2002; Nixon & King 2012; Shi et al. 2012; D'Orazio, Haiman & MacFadyen 2013; Farris et al. 2014; Muñoz et al. 2019; Alves et al. 2019). These streams are responsible for forming and replenishing circumstellar discs around each binary component. The accretion of material onto the circumstellar discs may aid in the formation of *S*-type planets, those that orbit one component of a binary. Accretion of material onto the central binary may be suppressed for small disc aspect ratios.

The structure of a circumstellar disc around one star is strongly affected by the tidal field of the binary companion (Papaloizou & Pringle 1977; Artymowicz & Lubow 1994; Pichardo, Sparke & Aguilar 2005; Jang-Condell 2015). Circumstellar discs around each binary component undergo tidal truncation. A circumstellar disc in a circular orbit binary is typically truncated to about one-third to one-half of the binary orbital separation The tidal truncation radius is expected to decrease with increasing binary eccentricity.

Kozai–Lidov (KL) oscillations (Kozai 1962; Lidov 1962) have been studied extensively to analyse several astronomical processes involving bodies that orbit a member of a binary system that begin on highly misaligned orbits. During KL oscillations, the object's inclination is exchanged for eccentricity, and vice versa. These processes include asteroids and irregular satellites (Kozai 1962; Nesvorný et al. 2003), artificial satellites (Lidov 1962), tidal disruption events (Chen et al. 2011), formation of Type Ia supernovae (Kushnir et al. 2013), triple star systems (Eggleton & Kiseleva-Eggleton 2001; Fabrycky & Tremaine 2007), planet formation with inclined stellar companions (Wu & Murray 2003; Takeda & Rasio 2005), giant outbursts in Be/X-ray binaries (Martin et al. 2014a; Martin & Franchini 2019), inclined planetary companions (Nagasawa, Ida & Bessho 2008), mergers of binaries in galactic nuclei (Blaes, Lee & Socrates 2002; Antonini & Perets 2012; Hamers et al. 2018; Hoang et al. 2018; Fragione et al. 2019a; Fragione, Leigh & Perna 2019b), stellar compact objects (Thompson 2011), and blue straggler stars (Perets & Fabrycky 2009).

A highly misaligned initially circular disc around one component of a binary undergoes KL cycles in which its inclination is exchanged for eccentricity, and vice versa (Martin et al. 2014a). Due to disc dissipation by viscosity and shocks, these oscillations are typically significantly damped after a few oscillations. KL oscillations can occur in a fluid disc with a wide variety of disc and binary parameters (Fu, Lubow & Martin 2015a). When the disc becomes eccentric, it overflows its Roche lobe and transfers material to the companion star (Franchini, Martin & Lubow 2019a). Self-gravity of a disc can suppress disc KL oscillations if the disc is close to being gravitationally unstable (Fu, Lubow & Martin 2015b). KL oscillations in a circumstellar disc may have significant consequences for planet formation since strong shocks in the gas are produced during high-eccentricity phases (Fu, Lubow & Martin 2017).

A misaligned circumbinary disc may form misaligned circumstellar discs around the individual binary components (e.g. Nixon et al. 2013; Smallwood, Martin & Lubow 2021b). A highly misaligned disc around one component of a binary may be unstable to the Kozai–Lidov (KL) mechanism (Martin et al. 2014a). Smallwood et al. (2021b) simulated the flow of gas originating from an initially misaligned circumbinary disc by 60°. The misaligned gas streams that flow into the binary cavity result in formation of highly tilted circumstellar discs around each binary component. The inclined circumstellar discs in turn undergo KL oscillations. However, the KL oscillations are long-lived, due to the continuous accretion of inclined material from the circumbinary disc. Long-lived KL cycles have important implications for planet formation in binary systems.

In this work, we extend the previous study Smallwood et al. (2021b) and consider more highly inclined circumbinary discs.

We first revisit the dynamics of highly inclined test particle orbits around one component of a binary in Section 2. In Section 3, we describe the setup for our hydrodynamical simulations. In Section 4, we discuss the results of our circumprimary disc simulations. We simulate a highly inclined circumprimary disc in a binary to explore the dynamics of the KL cycles. Previous studies have only dealt with circumprimary disc inclinations $\lesssim 60^\circ$, while we consider higher tilts, including a polar circumprimary disc. In Section 5, we show the results of our hydrodynamical simulations with an initial circumbinary disc, where we consider the flow of material from discs with various initial misalignments, including a polar circumbinary disc. Finally, a summary is given in Section 6.

2 KOZAI–LIDOV OSCILLATIONS OF TEST PARTICLES

Before considering discs, we consider the properties of test particle orbits that undergo KL oscillations. As a consequence of the conservation of the component of the angular momentum that is perpendicular to the binary orbital plane, the test particle's inclination is recurrently exchanged for eccentricity. This conservation is expressed as

$$\sqrt{1 - e_{\rm p}^2} \cos i_{\rm p} \approx {\rm const}, \tag{1}$$

where $i_{\rm p}$ is the particle inclination with respect to the binary orbital plane and $e_{\rm p}$ is the eccentricity of the test particle. A initially circular orbit particle initially gains eccentricity while reducing its orbital tilt (i.e. going towards alignment which means higher values of $|\cos i_{\rm p}|$) and then circularizes while gaining orbital tilt back to its original inclination. For an initially circular orbit particle, KL oscillations only occur if the initial tilt of the test particle $i_{\rm p0}$ satisfies $\cos^2 i_{\rm p0} < \cos^2 i_{\rm cr} = 3/5$ (Innanen et al. 1997), which requires that $39^\circ \lesssim i_{\rm p0} \lesssim 141^\circ$. From equation (1), an initially circular particle orbit can achieve a maximum eccentricity given by

$$e_{\rm max} = \sqrt{1 - \frac{5}{3}\cos^2 i_{\rm p0}}. \tag{2}$$

The increase in a circular particle's eccentricity can be quite significant. For example, if the particle's initial orbit is tilted by 60°, the maximum eccentricity reached during a KL cycle is about 0.75.

For eccentric binaries, stronger effects from KL oscillations have been found to exist (Ford, Kozinsky & Rasio 2000; Lithwick & Naoz 2011; Naoz et al. 2011, 2013a, b; Teyssandier, Terquem & Papaloizou 2013; Li et al. 2014; Liu, Muñoz & Lai 2015). The KL oscillation period for a particle in the potential of an eccentric binary is approximately given by

$$\frac{\tau_{\rm KL}}{P_{\rm b}} \approx \frac{M_1 + M_2}{M_2}\frac{P_{\rm b}}{P}(1 - e_{\rm b}^2)^{3/2}, \tag{3}$$

(Holman, Touma & Tremaine 1997; Innanen et al. 1997; Kiseleva, Eggleton & Mikkola 1998), where M_1 and M_2 are the masses of the primary and secondary components of the binary, respectively, $P = 2\pi/\sqrt{GM_1/a_{\rm p}^3}$ is the orbital period of the particle with semimajor axis $a_{\rm p}$, $P_{\rm b} = 2\pi/\Omega_{\rm b}$ is the orbital period of the binary, $e_{\rm b}$ is the binary eccentricity, and $\Omega_{\rm b} = \sqrt{G(M_1 + M_2)/a_{\rm b}^3}$ is the binary orbital frequency for binary semimajor axis $a_{\rm b}$.

To simulate an inclined circumprimary test particle in a binary, we use the N-body integrator, MERCURY (Chambers 1999). The test particle is orbiting the primary companion with an initial tilt i_0 relative to the binary orbital plane. The binary components have equal mass so that $M_1 = M_2 = M/2$, where M is the total mass of the binary. Fu et al. (2015b) ran numerous test particle orbits showing the effects the particle and binary parameters have on the induced KL oscillations. Following their work, we model an eccentric inclined particle around one component of an eccentric binary, more applicable to binary systems.

We first simulate an inclined particle in a circular binary to match previous results. Fig. 1 shows the eccentricity and inclination of a circumprimary particle as a function of time that begins on a circular orbit. The analytic solution for these test particle orbits in the quadrupole approximation is given in Lubow (2021). We consider various initial tilts of the test particle orbit. The critical inclination that the test particle orbit must have to induce KL cycles is ∼39°. Thus, a particle tilt of 30° (black line) does not undergo KL oscillations. As the initial inclination of the particle increases, the KL oscillations become more frequent, and the growth in the eccentricity becomes more prominent (in agreement with Fig. 1 in Fu et al. (2015b)). The trough in the inclination profile of a test particle becomes narrower with initial inclination. An initial particle orbit tilt of 90° becomes unstable and collides with the primary star during the first KL oscillation because the particles eccentricity exceeds 1.0. The eccentricity of the polar particle increases almost up to its maximum eccentricity before the tilt begins to change.

Next, we set the initial particle tilt to 60° around a slightly eccentric binary with $e_{\rm b} = 0.1$, as we will consider in the disc simulations. We model various initial test particle eccentricities ranging from 0.0 to 0.5. Fig. 2 shows the eccentricity and inclination of eccentric circumprimary particles as a function of time in binary orbital periods. An inclined circular test particle within an eccentric binary has an increased frequency in KL oscillations when compared to a particle orbiting one component of a circular binary, as expected by equation (3). From Fig. 2, when the particle eccentricity is increased, the maximum eccentricity reached during a KL oscillation also increases. However, the difference between the initial eccentricity to the maximum eccentricity of the particle decreases as the initial particle eccentricity increases.

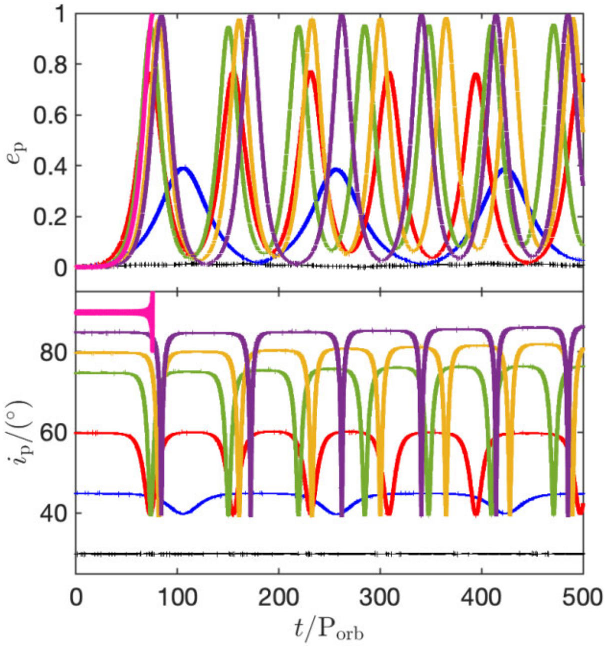

Figure 1. Eccentricity (upper panel) and inclination (lower panel) evolution of circumprimary test particles under the influence of a circular binary for initially circular orbit particles. We vary the initial particle orbital tilt, i_0, beginning with 30° (black), 45° (blue), 60° (red), 75° (green), 80° (yellow), 85° (purple), and 90° (pink). The initial orbital radius of the particle is set at $r_0 = 0.06a$, where a is the separation of the binary. The time is in units of binary orbital period $P_{\rm orb}$.

Lastly, we examine the KL mechanism for a nearly polar particle. From Fig. 1, an initially circular orbit particle with an initial orbital tilt of 85° is unstable to KL oscillations but is otherwise stable. We consider a nearly polar orbit particle with an initial orbital tilt $i_0 = 85^\circ$ around a binary with eccentricity $e_{\rm b} = 0.1$. In Fig. 3 we show the particle eccentricity and inclination as a function of time in binary orbital periods. The various lines correspond to different initial particle eccentricities ranging from 0.0 to 0.5. For all values of the initial particle eccentricity we consider, the particle proceeds through KL cycles in a periodic fashion. Unlike the particle beginning at a tilt of 60°, a nearly polar particle exhibits similar maximum eccentricity close to unity during a KL oscillation regardless of initial particle eccentricity. The minimum inclination reached during each KL oscillation is roughly independent of particle initial eccentricity.

3 HYDRODYNAMICAL-SIMULATION SETUP

We use the smoothed particle hydrodynamics (SPH) code PHANTOM (Price et al. 2018a) to model gaseous circumbinary and circumstellar discs. PHANTOM has been tested extensively for modelling misaligned

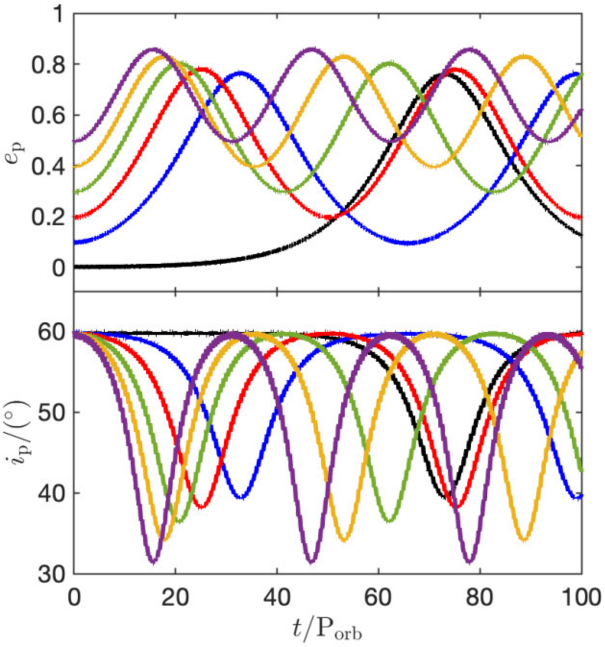

Figure 2. Eccentricity (upper panel) and inclination (lower panel) evolution of circumprimary test particles under the influence of binary with eccentricity $e_b = 0.1$. The initial tilt of the particle orbit is set to 60°. We vary the initial particle eccentricity e_0 beginning with $e_0 = 0$ (black), 0.1 (blue), 0.2 (red), 0.3 (green), 0.4 (yellow), and 0.5 (purple). The initial orbital radius of the particle is set at $r_0 = 0.06a$, where a is the separation of the binary. The time is in units of binary orbital period $P_{\rm orb}$.

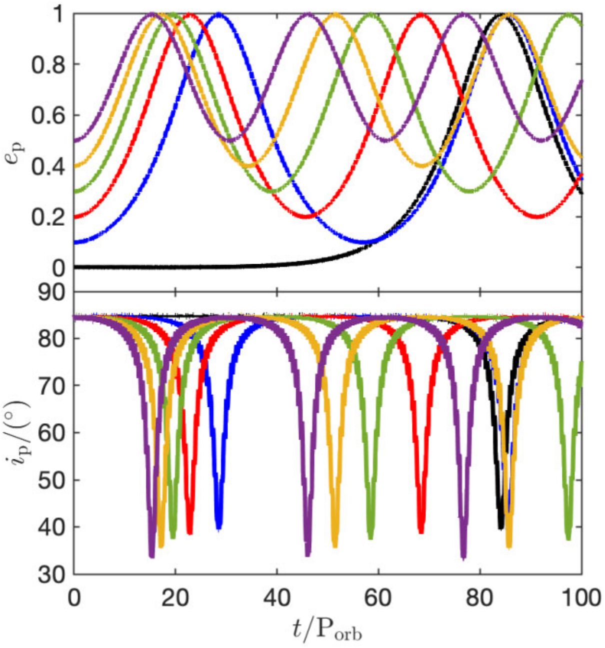

Figure 3. Same as Fig. 2 but for nearly polar test particles with an initial orbital tilt $i_0 = 85°$.

circumbinary discs (Nixon 2012; Nixon et al. 2013; Nixon & Lubow 2015; Facchini, Juhász & Lodato 2018; Smallwood et al. 2019; Poblete, Cuello & Cuadra 2019; Smallwood et al. 2020; Aly & Lodato 2020; Hirsh et al. 2020; Smallwood et al. 2021b), as well as misaligned circumstellar discs around individual binary components (e.g. Martin et al. 2014b; Doğan et al. 2015; Franchini, Martin & Lubow 2020). The suite of simulations is summarized in Table 1. In this section we describe the setup for the binary star, circumprimary disc, and circumbinary disc in further detail.

3.1 Binary star setup

We model the binary star system as a pair of sink particles, with an initial binary separation a. The binary is not static but rather evolves freely in time. Each sink particle is given an initial mass with M_1 being the primary mass and M_2 being the secondary mass. The total binary mass is thereby $M = M_1 + M_2$. All of our simulations assume an equal-mass binary ($M_1 = M_2$). In Cartesian coordinates, the orbit of the binary lies in the x–y plane initially. The binary begins initially at apastron along the x-axis. The massive sink particles have a hard accretion boundary, meaning that when particles penetrate the sink accretion radius, the particle's mass and angular momentum are deposited onto the star (e.g. Bate, Bonnell & Price 1995). A large accretion radius is often used to reduce the computation time significantly by neglecting to resolve close-in particle orbits. In this work, however, we are interested in resolving the formation and evolution of the circumstellar material. Therefore, we adopt a relatively small accretion radius of $0.05a$ for simulations that begin with a CBD and an accretion radius of $0.025a$ for simulations that begin with a CPD. Using a smaller accretion radius for the CPD simulations ensures that the disc lifetime is longer, along with higher disc resolution. The more eccentric the binary, the smaller the outer truncation radius for the circumstellar discs (Artymowicz & Lubow 1994). Having a small binary eccentricity helps with the resolution of the circumstellar discs. On the other hand, to have a stable polar CBD, the binary eccentricity needs to be a non-zero value. The initial binary eccentricity is set to $e_b = 0.1$, with the binary eccentricity vector along the positive x-axis. With this value of binary eccentricity, the critical tilt of the CBD to remain nearly polar is ∼77° (see equation 33 in Martin & Lubow 2019).

3.2 CPD setup

To model a CPD, we follow the methods of Martin et al. (2014b). Runs 1–5 in Table 1 simulate initially a CPD. The inner and outer disc radii are set at $r_{\rm in} = 0.025a$ and $r_{\rm out} = 0.25a$, respectively, with a initial total disc mass $M_{\rm CPD} = 10^{-3}\,M$. The CPD consists of 750 000 equal-mass Lagrangian particles. We neglect any effects of self-gravity. The disc surface density profile is initially a power-law distribution given by

$$\Sigma(r) = \Sigma_0 \left(\frac{r}{r_{\rm in}}\right)^{-p}, \quad (4)$$

where we set $p = 3/2$. We adopt a locally isothermal disc with sound speed $c_s \propto R^{-3/4}$, $H/r = 0.035$ at $r = r_{\rm in}$, and $H/r = 0.02$ at $r = r_{\rm out}$. With this prescription, the viscosity parameter α and $\langle h\rangle/H$ are effectively constant over the radial extend of the disc (Lodato & Pringle 2007). For the CPD simulations, we take the Shakura & Sunyaev (1973) α parameter to be 0.01. To accomplish this, the SPH artificial viscosity coefficients are set as $\alpha_{\rm AV} = 0.18$ and $\beta_{\rm AV} = 2.0$. The disc is resolved with shell-averaged smoothing length per scale height $\langle h\rangle/H \approx 0.55$.

3.3 CBD setup

To model an initially flat but tilted gaseous CBD, we follow the methods of Smallwood et al. (2021b). Runs 6, 7, and 8 in Table 1

Table 1. The setup of the SPH simulations that includes an initial circumprimary disc (CPD) or circumbinary disc (CBD).

Model	Disc Setup	$i_0/^\circ$	$r_{\rm in}/a$	$r_{\rm out}/a$	α	$H/r_{\rm in}$	$H/r_{\rm out}$	# Particles	KL unstable?
run1	CPD	60	0.025	0.25	0.01	0.035	0.02	750 000	Yes
run2	CPD	70	0.025	0.25	0.01	0.035	0.02	750 000	Yes
run3	CPD	80	0.025	0.25	0.01	0.035	0.02	750 000	Yes
run4	CPD	90	0.025	0.25	0.01	0.035	0.02	750 000	Yes
run5	CPD	100	0.025	0.25	0.01	0.035	0.02	750 000	Yes
run6*	CBD	60	1.6	2.6	0.1	0.1	0.088	1.5×10^6	Yes
run7	CBD	60	1.6	2.6	0.1	0.1	0.088	750 000	Yes
run8	CBD	90	1.6	2.6	0.1	0.1	0.088	1.5×10^6	Yes

The table lists the initial parameters beginning with the disc tilt i_0, inner disc radius $r_{\rm in}$, outer disc radius $r_{\rm out}$, α viscosity parameter, disc aspect ratio at inner disc radius $H/r_{\rm in}$, disc aspect ratio at outer disc radius $H/r_{\rm out}$, the number of particles, and whether or not the circumstellar discs undergo the Kozai–Lidov (KL) instability. *Note.** Simulation from Smallwood et al. (2021b)

describe the simulations of a CBD. The disc initially consists of 1.5×10^6 equal-mass Lagrangian SPH particles. We also model a 750 000 particle simulation for a resolution study. The simulations run for 45 $P_{\rm orb}$, where $P_{\rm orb}$ is the orbital period of the binary. This is sufficient time for the forming circumstellar discs to reach a quasi-steady state. We simulate initially highly misaligned disc inclinations of $i_0=60^\circ, 90^\circ$. A disc with $i_0=90^\circ$ is in a polar configuration, where the angular momentum vector of the disc is aligned to the eccentricity vector of the binary. At the beginning of our simulations, we select an initial inner disc radius, $r_{\rm in}$, and outer disc radius, $r_{\rm out}$, where the initial total disc mass, $M_{\rm CBD}$, is confined. All of the simulations model a low-mass CBD such that $M_{\rm CBD}=10^{-3}\,M$. We choose the CBD to be radially very narrow and close to the binary orbit. This is done to maximize the accretion rate onto the binary and hence the resolution of the circumstellar discs (e.g. Smallwood et al. 2021b). For our simulations, we take $r_{\rm in}=1.6a$ and $r_{\rm out}=2.6a$. The tidal torque is weaker at a given radius for a more highly misaligned disc which allows the inner disc radius to lie closer to the binary than a coplanar disc (e.g. Lubow et al. 2015; Miranda & Lai 2015; Lubow & Martin 2018). The inner truncation radius of a polar CBD is around 1.6 a (Franchini et al. 2019b), much smaller than the $2-3\,a$ expected for coplanar discs (Artymowicz & Lubow 1994).

The disc surface density profile follows from equation (4). The physical disc viscosity is incorporated by using artificial viscosity $\alpha^{\rm av}$, which is detailed in Lodato & Price (2010). By using our surface density profile and a disc aspect ratio $H/r=0.1$ at $r_{\rm in}$, the shell-averaged smoothing length per scale height $\langle h\rangle/H$ and the disc viscosity parameter α are constant over the radial extent of the disc (Lodato & Pringle 2007). The CBD is initially resolved with $\langle h\rangle/H \approx 0.11$. The parameters for the simulations require a high viscosity in order to maximize the accretion rate on to the circumstellar discs and provide better resolution. We consider a relatively high value for the Shakura & Sunyaev (1973) $\alpha_{\rm SS}$ of 0.1. In a more realistic system, the disc viscosity may be lower.

In order to more accurately simulate the formation and development of circumstellar discs, we adopt the locally isothermal equation of state of Farris et al. (2014) and set the sound speed $c_{\rm s}$ to be

$$c_{\rm s}=\mathcal{F}c_{\rm s0}\left(\frac{a}{M_1+M_2}\right)^q\left(\frac{M_1}{r_1}+\frac{M_2}{r_2}\right)^q, \tag{5}$$

where r_1 and r_2 are the radial distances from the primary and secondary stars, respectively, and $c_{\rm s0}$ is a constant with dimensions of velocity. q is set to 3/4. $\mathcal{F}$ is a dimensionless function of position that we define below. This sound speed prescription guarantees that the temperature profiles in the circumprimary and circumsecondary discs are set by the primary and secondary stars, respectively. For r_1, $r_2\gg a$, $c_{\rm s}$ is set by the distance from the binary centre of mass.

To increase the resolution of the circumstellar discs, we include a function $\mathcal{F}$ in equation (5) as detailed in Smallwood et al. (2021b). The purpose of $\mathcal{F}$ is to modify the sound speed around each binary component so that the viscous time-scale is longer. This increases the mass (and hence the resolution) in the steady-state circumstellar discs. We take

$$\mathcal{F}=\begin{cases}\sqrt{0.001}, & \text{if } r_1 \text{ or } r_2<r_{\rm c},\\ 1, & \text{otherwise},\end{cases} \tag{6}$$

where $r_{\rm c}$ is the cutoff radius. We set a cutoff radius of $r_{\rm c}=0.35a$ from each binary component (e.g. Smallwood et al. 2021b). Using the prescription mentioned above ensures that the disc aspect ratio of the circumstellar discs at radius $r=0.1a$ is $H/r\sim0.01$, which is one-tenth of the disc aspect ratio at the initial inner CBD radius.

3.4 Analysis routine

We analyse the disc and binary parameters as a function of time. The parameters include tilt, eccentricity, the longitude of the ascending node, mass, and mass accretion rate. To probe the CPD simulations, we average over particles in the radial range from $0.025a$ to a distance of $0.30a$. For the CBD simulations, we average over particles in the radial range from $1.4a$ to a distance of $10a$. For the forming circumstellar discs, we average over all particles bound to each binary component (i.e. the specific energies, kinetic plus potential, of the particles are negative, neglecting the thermal energy). The tilt, i, is defined as the angle between the initial angular momentum vector of the binary (the z-axis) and the angular momentum vector of the disc. The longitude of the ascending node, ϕ, is measured relative to the x-axis (the initial binary eccentricity vector).

4 HYDRODYNAMICAL RESULTS WITH A CPD

This section considers the evolution of a CPD in the absence of accretion from a CBD. This enables us to disentangle the effect of accretion onto the circumstellar discs. We focus on large CPD misalignments in an eccentric binary star system. We consider five different initial disc tilts, 60° (run1 from Table 1), 70° (run2), 80° (run3), 90° (run4), and 100° (run5). Fig. 4 shows the disc tilt, eccentricity, the longitude of the ascending node, the mass of the CPD, and the accretion rate onto the primary star as a function of time in binary orbital periods. The disc exhibits KL cycles for each initial tilt, where the disc eccentricity and inclination are exchanged. For a disc with an initial tilt of 60°, Martin et al. (2014a) found that the first KL oscillation occurred around 10 $\mathrm{P}_{\rm orb}$ for a circular binary.

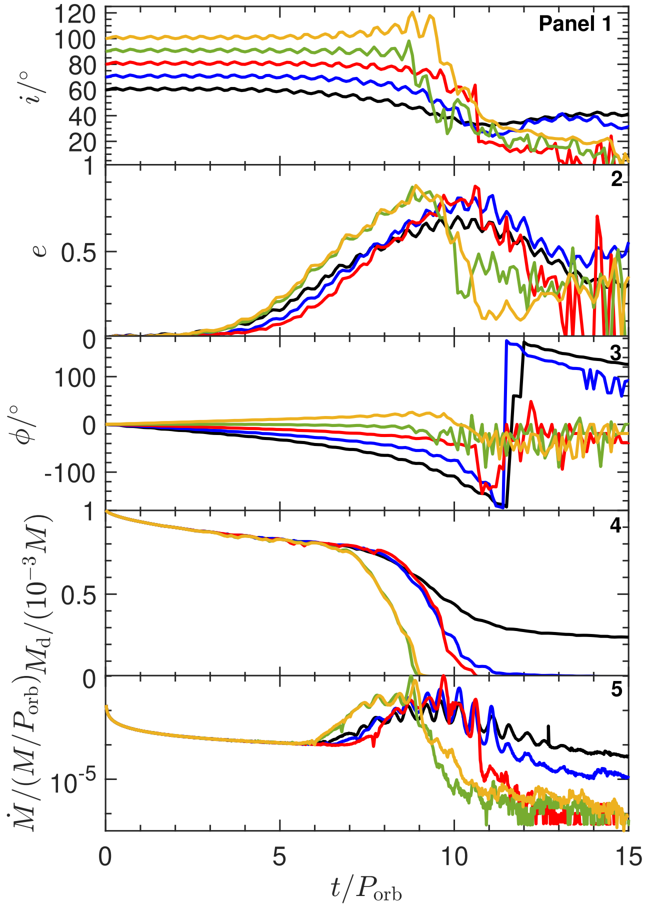

Figure 4. Evolution of a KL unstable CPD as a function of time in units of the binary orbital period $P_{\rm orb}$. We simulate five different initial disc inclinations, which are 60° (run1 from Table 1, black), 70° (run2, blue), 80° (run3, red), 90° (run4, green), and 100° (run5, yellow). The disc parameters are tilt i (panel 1), eccentricity e (panel 2), longitude of the ascending node ϕ (panel 3), and disc mass $M_{\rm d}$ (panel 4). The mass accretion rate $\dot{M}$ onto the primary star is shown in panel 5.

In our case, the disc with the same initial tilt undergoes the first KL oscillation much sooner due to the binary having a slightly eccentric orbit (see Fig. 12 in Fu et al. 2015a). Due to viscous dissipation and the lack of circumbinary material, the KL oscillations damp quickly in time. For higher initial inclinations, 70°, 88°, 90°, and 100°, the discs do not survive after one KL oscillation for our given sink size. The discs become very eccentric, which leads to the majority of the disc material being accreted by the primary star. Increasing the resolution of these simulations does not lengthen the disc lifetime. However, if we were to use a smaller sink size, then the disc could survive through the KL oscillations. A smaller sink size would ensure that a larger portion of the disc could survive. An accretion radius of ~ 0.01 au is comparable to the size of the star, but we simulate a larger sink size for computational reasons and to compare with the CBD simulations detailed in the next section. The initially polar disc's tilt does not change much from polar before the majority of the disc is accreted. This is likely a consequence of the high disc eccentricities that are developed which is consistent with the results for test particle orbits (see Fig. 1). In the retrograde case, $i_0 = 100°$, as the disc eccentricity increases, the inclination also increases, opposite to the prograde cases.

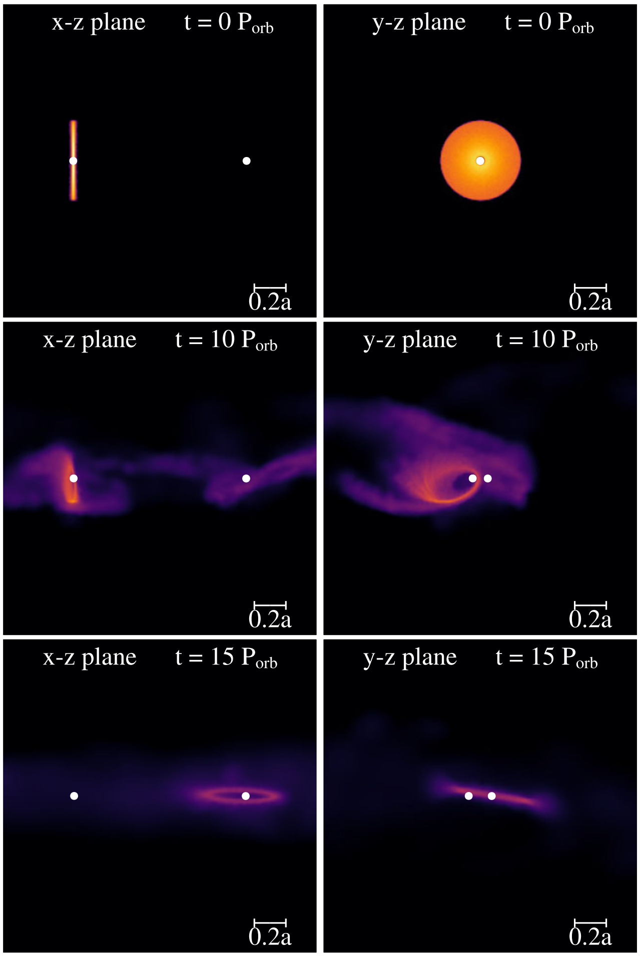

Figure 5. The evolution of polar CPD (run4 from Table 1). The white circles denote the eccentric orbit binary components with an initial binary separation of a. The top row shows the initial disc setup. The middle and bottom rows show the disc evolution at $t = 10\ P_{\rm orb}$ and $t = 15\ P_{\rm orb}$, respectively, where $P_{\rm orb}$ is the binary orbital period. The colour denotes the gas surface density, with the orange regions being about three orders of magnitude larger than the purple regions. The left column shows the x–z plane, and the right column shows the y–z plane. At $t = 10\ P_{\rm orb}$, the CPD is highly eccentric due to the Kozai–Lidov instability. Also, at this time, a circumsecondary disc is being formed from material flowing close to the secondary binary component from the eccentric CPD. At $t = 15\ P_{\rm orb}$, the CPD has completely dissipated from being accreted onto the primary star and transferring material to the secondary star. At this time, there is more material in the newly formed circumsecondary disc.

Highly inclined particle orbits experience a large (nearly 180°) shift in ϕ within a small time interval centered about the eccentricity maximum (see the plot for $\Omega(t)$ in Fig. 1 of Lubow (2021)). This large shift does not appear in Fig. 4 or in any of our other phase results. We are not sure why this is the case. Perhaps the disc is unable to respond to such a large shift within a short time.

We further examine the evolution of the polar ($i_0 = 90°$) CPD. In Fig. 5, we show the polar CPD structure at three different times, $t = 0\ P_{\rm orb}$, $10\ P_{\rm orb}$, and $15\ P_{\rm orb}$. Initially, the polar disc around the primary star (left white dot) is edge-on in the x–z plane and face-on y–z plane. At $t = 10\ P_{\rm orb}$, the disc is at peak eccentricity growth from the KL instability. Also, at this time, streams of material from the CPD flow around the secondary star (right white dot) and begin forming a circumsecondary disc. At $t = 15\ P_{\rm orb}$, the CPD has dissipated due

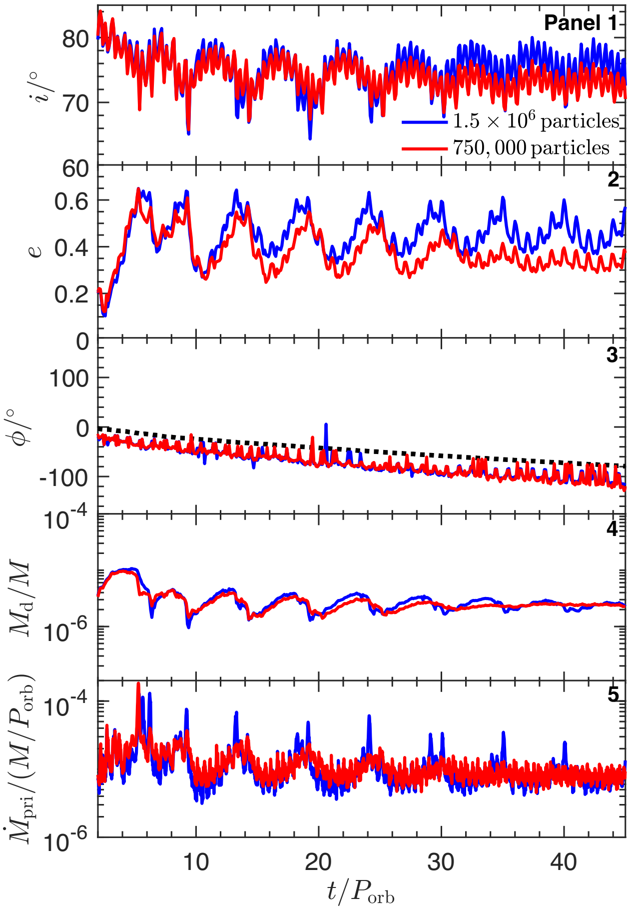

Figure 6. Resolution study for a CBD that is initially misaligned by 60°. The blue curves represent the simulation with initially 1.5×10^6 particles in the CBD, while the red curves denotes the simulation with initially 750 000 particles. The first four panels show the disc parameters for the newly forming CPD as a function of time in units of the binary orbital period, $P_{\rm orb}$. The disc parameters are tilt i (panel 1), eccentricity e (panel 2), longitude of the ascending node ϕ (panel 3), and disc mass $M_{\rm d}$ (panel 4). The black-dotted curve in the third panel denotes the CBD. The lower panel shows the mass accretion rate onto the primary star $\dot{M}_{\rm pri}$ (panel 5).

to accretion onto the primary star and transporting material to the circumsecondary disc. The newly formed circumsecondary disc is at a lower tilt, below the threshold, to induce the KL cycles.

5 HYDRODYNAMICAL RESULTS WITH A CBD

In this section, we examine how misaligned and polar circumbinary material flows through the binary cavity and forms circumstellar discs around each binary component. We first conduct a resolution study of our earlier work from Smallwood et al. (2021b), modelling an initially 60° misaligned CBD. We then focus on the polar CBD case.

5.1 Resolution Study

We examine a CBD with an initial misalignment of $i_0 = 60^\circ$ with two different initial numbers of particles, 1.5×10^6 (run6) and 750 000 (run7). The upper four panels in Fig. 6 show the CPD parameters as a function of time. The bottom panel shows the mass accretion rate onto the primary star. The blue curves represent the 1.5×10^6 particle simulation, while the red curves represent the 750 000 particle simulation. Panels 1 and 2 show the evolution of disc eccentricity and inclination where the forming CPD undergoes KL oscillations from the continuous accretion of material from the CBD. The oscillations damp in time at both resolutions, with the lower resolution simulation damping more quickly. Therefore, the oscillations are likely limited by resolution. If the accretion time-scale is long compared to the KL time-scale, we expect the KL oscillations to damp over time, similar to the CPD simulations without accretion shown in the previous Section. If the accretion time-scale is short compared to the KL time-scale, there should be no KL oscillations present. In this case, the material moves through the disc faster than it becomes unstable to KL oscillations. We expect the optimal oscillations when the time-scales are comparable because the disc refills mass on the time-scale that the oscillations take place. For the simulation with a 60° tilted CBD, the accretion time-scales for the primary and secondary are $\sim 1.5\,{\rm P_{orb}}$, whereas the KL time-scale for this simulation is $\sim 5\,{\rm P_{orb}}$. The simulation is in the regime where the accretion time-scale is shorter than the KL oscillation time-scale because when the disc becomes eccentric during the KL oscillations, a large amount of disc material is accreted, reducing the accretion time-scale. However, the accretion time-scale is dependent on the disc viscosity. In our hydrodynamical simulations, we use an artificial viscosity to model an expected Shakura & Sunyaev (1973) viscosity coefficient. The number of Lagrangian particles determines how close the artificial viscosity is to the actual value. Thus, the α is artificially higher at lower resolutions, leading to a shorter accretion time-scale. For our higher-resolution simulation, the α is lower, leading to a longer accretion time-scale.

Panel 3 in Fig. 6 shows the longitude of the ascending node as a function of time. The precession rate of the CPD is only slightly faster than the CBD on average. In the absence of the effects of KL oscillations, the nodal precession rate of the primary disc, assuming constant surface density Σ out to disc radius r from the primary, is given by

$$\omega_{\rm pr} = -\frac{15 M_2 r^3}{32 M_1 a_{\rm b}^3} \cos{(i)}\, \Omega(r), \qquad (7)$$

where i is inclination angle of the primary disc relative to the binary orbital plane and $\Omega = \sqrt{G M_1/r^3}$ is the angular velocity in the disc (Larwood et al. 1996). With $r = 0.35\,a_{\rm b}$, we find $\omega_{\rm pr} = 6^\circ/P_{\rm orb}$ with a revolution period of $\sim 56\,{\rm P_{orb}}$. Therefore, the circumstellar discs should have nodally precessed 75 per cent of a revolution in $45\,{\rm P_{orb}}$. In panel 3 we see that the circumstellar discs have only completed roughly 30 per cent of a nodal revolution. It is possible that the circumprimary phase is affected by the phase of accreted gas from the CBD that undergoes relatively slow nodal precession. As discussed in Section 4, KL oscillations modify the nodal precession rate of a test particle in a way that we do not see in the disc simulations. Lastly, the mass in the CPDs oscillates in time, with the troughs corresponding with each high eccentricity period. During each high eccentricity phase, the accretion rate peaks as seen in panel 5.

5.2 Polar discs

In this section, we present a hydrodynamical simulation of the flow of material from a polar CBD onto the binary components (run8). The top row of Fig. 7 shows the initial configuration of the polar CBD around an eccentric binary. The bottom row shows the disc structure at $t = 25\ P_{\rm orb}$. The CBD remains nearly polar ($\sim$90°) as shown in the x–z plane. Material flows from the polar CBD and forms nearly polar circumstellar discs around each binary component. The cavity size

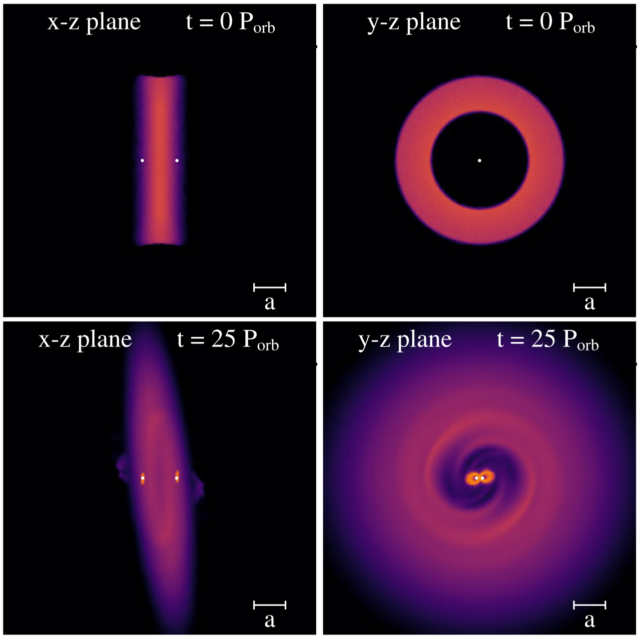

Figure 7. The formation of polar circumstellar discs from an initially low-mass polar CBD (run8). The white circles denote the eccentric orbit binary components with an initial binary separation of a. The upper panels denote the initial disc setup, while the bottom panels show the disc evolution at $t = 25\ P_{\rm orb}$, where $P_{\rm orb}$ is the binary orbital period. At this time, nearly polar circumstellar discs are forming around each binary component. The colour denotes the gas density using a weighted density interpolation, which gives a mass-weighted line of sight average. The yellow regions are about three orders of magnitude larger than the purple. The left column shows the x–z plane, and the right column shows the y–z plane.

is smaller in the polar disc compared to a coplanar disc simulation as expected (Lubow et al. 2015; Miranda & Lai 2015).

The upper four panels in Fig. 8 show the inclination, eccentricity, the longitude of the ascending node, and disc mass for the three discs as a function of time in binary orbital periods. The lower panel shows the mass accretion rate onto the sinks. The circumstellar discs form at a time of $\sim 10\,\mathrm{P_{orb}}$, later than in the simulation with a lower level of CBD misalignment. The CBD tilt evolves in time. Since we model a disc with a non-zero mass, it will align to a generalized polar state with an inclination that is $<90^\circ$ (e.g. Martin & Lubow 2019; Chen et al. 2019). In this case, the circumstellar discs form slightly retrograde, with a tilt just above 90°. The primary and secondary discs form with an eccentricity of $\sim$0.25. However, the polar circumstellar discs undergo the KL instability, which forces the disc eccentricity and tilt to oscillate in time. Looking at panels 1 and 2, we see that as the disc eccentricity increases, the disc tilt also increases, the opposite of the conventional KL case involving prograde orbits. However, this result is consistent with the KL mechanism for retrograde orbits. Panel 3 shows the evolution of the longitude of the ascending node in time. Since the circumprimary and circumsecondary discs are nearly polar, they exhibit very little precession (see equation 7 and discussion below it). The mass of the polar circumstellar discs oscillates in time (panel 4), likely due to the oscillating disc eccentricity. The polar CBD has lost $\sim$25 per cent of its initial mass.

The KL oscillations from Fig. 8 damp in time. However, from our resolution study, the damping is primarily due to the initial number of particles. The accretion time-scale for this simulation is $\sim 15\,\mathrm{P_{orb}}$, and the KL time-scale in this case is $\sim 10\,\mathrm{P_{orb}}$. The accretion time-scale is longer in the polar simulation than in the 60° simulation because the polar circumstellar discs become less eccentric during each KL cycle, accreting less disc material. For a higher resolution, we expect the KL oscillations to be long-lived even for polar circumstellar discs.

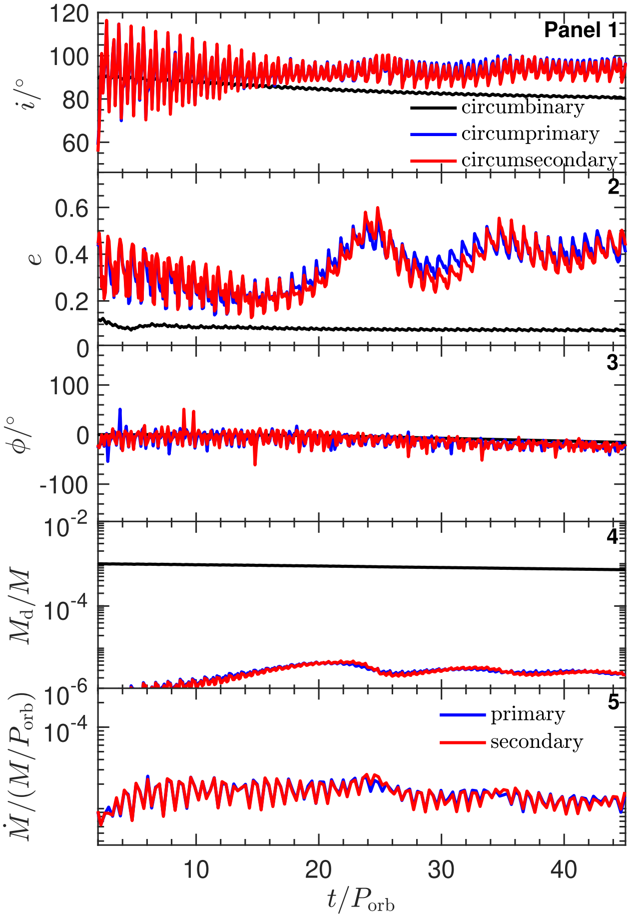

Figure 8. Simulation results for run8 for an initially polar CBD. The disc parameters are shown for the circumprimary, circumsecondary, and circumbinary disc as a function of time in units of the binary orbital period, $P_{\rm orb}$. The upper four panels show the disc tilt i (panel 1), eccentricity e (panel 2), longitude of the ascending node ϕ (panel 3), and disc mass $M_{\rm d}$ (panel 4) for the three discs. The lower panel shows the mass accretion rate onto the sinks $\dot{M}$ (panel 5).

On the bottom-left panel in Fig. 7, we see that some material is flung out of the disc plane on both sides of the polar CBD. This material forms two lobes on both sides of the disc. Fig. 9 shows the edge-on view of the disc surface density, along with the velocity vectors. The material is being flung outwards but remains bound to the binary. Therefore, the material then falls back into the gap region of the CBD. Throughout the simulation, the material is periodically flung out every $0.5\ P_{\rm orb}$ when the binary components pass through the polar CBD plane.

We further examine the flow of polar circumbinary material onto the forming circumstellar discs. First, we investigate the tilt of the gaseous streams that accrete onto the circumstellar discs as a function of time. Fig. 10 shows the CBD tilt as a function of disc radius. The inner edge of the disc lies roughly at $1.6a$. The curves that are shown at radii $<1.6a$ map the tilt of the streams. We show the disc tilt for a full binary orbital period from $20\,\mathrm{P_{orb}}$ to $21\,\mathrm{P_{orb}}$ in increments

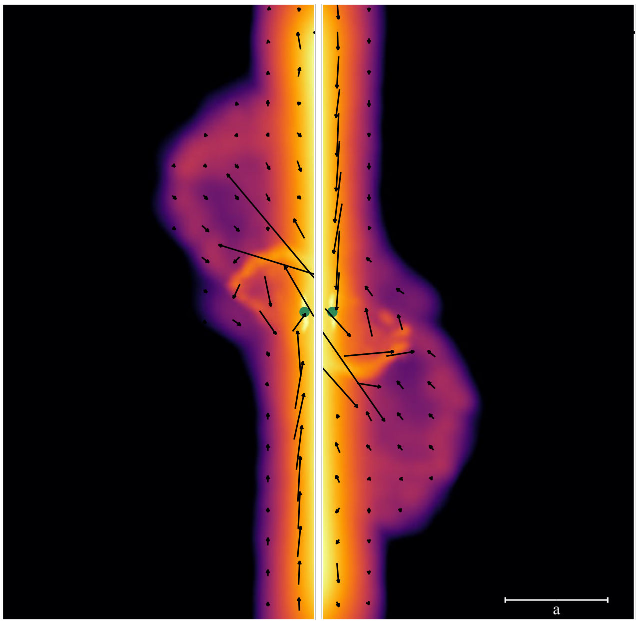

Figure 9. Edge-on view (x–z plane) of a polar CBD (run8) at a time $t = 5\,P_{\rm orb}$. We ignore the main portions of the disc confined within $r < 0.45a_{\rm b}$, where $a_{\rm b}$ is the separation of the binary. The binary components are shown as the green dots. The colours denote the disc surface density, with the orange regions being about three orders of magnitude larger than the purple regions. We overlay the velocity vectors shown by the black arrows. The length of the arrow is proportional to the velocities of the particles. We see two asymmetric lobes of material that are produced by the binary. Several of the velocity vectors are directed away from the plane of the CBD; however, the material then falls back onto the disc gap.

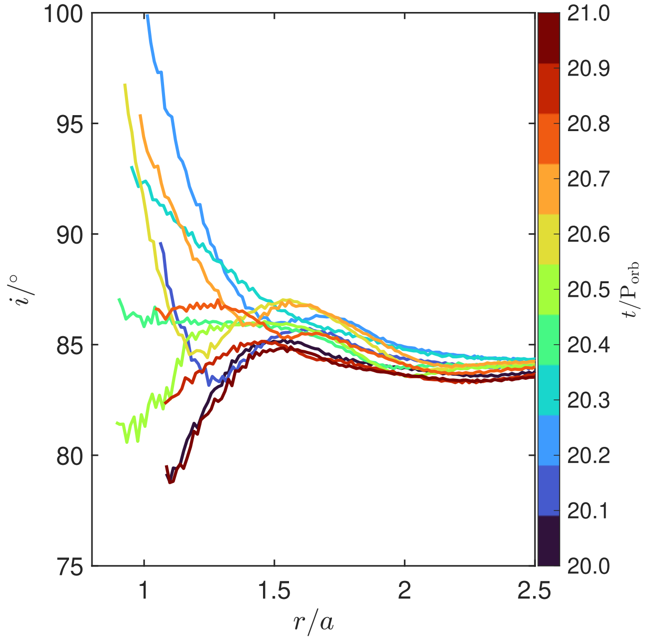

Figure 10. CBD tilt, i, as a function of radius, r, for the polar CBD. The colour corresponds to the time in binary orbital periods, $\rm P_{orb}$.

of $0.1\,\rm P_{orb}$. At every $0.5\,\rm P_{orb}$, the tilt of the streams are low at ∼80°. When the binary orbital period is not at half increments, the tilt of the streams increases beyond 90°. For example, at times $20.2 - 20.3\,\rm P_{orb}$ and $20.6 - 20.7\,\rm P_{orb}$, the streams are highly tilted. Recall that the forming circumstellar discs initially form at a high disc tilt, >90°. Therefore, whenever the gaseous streams are highly tilted, there is an increased accretion of material onto the circumstellar discs from the CBD. When the streams are less inclined, every $0.5\,\rm P_{orb}$, there will be less material accreted onto the polar circumstellar discs. This phenomenon is also consistent with Fig. 9, where material is flung out of the plane of the CBD every $0.5\,\rm P_{orb}$. We test this by further visualizing the inflow of material. Fig. 11 shows snapshots of zoomed-in views in the x–z and y–z planes of the disc surface density, showing the gaseous streams accreting onto the nearly polar circumstellar discs. The snapshots show the flow of material over $20\,\rm P_{orb}$ to $20.9\,\rm P_{orb}$ in increments of $0.1\,\rm P_{orb}$. Higher density streams occur at times $20.3\,\rm P_{orb}$ and $20.7\,\rm P_{orb}$. The flow of material decreases every $0.5\,\rm P_{orb}$ during the orbit. At these times, the steams are less dense, leading to less material accreting onto the circumstellar discs.

We relate the flow of material from Fig. 11 to the mass of the circumstellar discs. Fig. 12 shows the mass of the CPD from $20\,\rm P_{orb}$ to $25\,\rm P_{orb}$ folded on top of one another for each orbital period. The vertical dashed-lines denote the times when the binary is aligned with the CBD plane, which is assumed when the stars are both aligned with x–z plane. Each time the binary aligns to the plane of the disc, the masses of the circumstellar discs increase. The mass of the disc decreases every $0.5\,\rm P_{orb}$. This behaviour repeats every orbital period. Overall, the disc mass deceases in time due to the KL mechanism.

6 SUMMARY

In this work, we investigated the flow of material from a CBD that results in the formation circumstellar discs around each binary component. We simulated an initially highly misaligned and polar CBD using 3D SPH. We considered cases of low-initial binary eccentricity (typically $e_{\rm b} = 0.1$) and binary mass ratio of unity. We also simulated cases of test particles around the primary star and cases of CPDs only (i.e. no circumbinary or circumsecondary discs) for comparison.

In order to carry out these simulations in a reasonable amount of time, we made some compromises on our choice of parameters. In particular, we introduced a higher viscosity parameter for the CBD than is likely to occur and a lower temperature of the gas in the gap region. These choices were made to improve the resolution of the simulations. Even with these parameters, the resolution is still playing a role in our results (see Fig. 6). While we have chosen the disc parameters (α and H/R) in our simulations to maximize the accretion rate on to the binary components and therefore the simulation resolution, we expect the general behaviour to persist for more realistic parameters applicable to protoplanetary discs. The mass of the circumstellar disc scales with the infall accretion rate. If the resolution of the circumstellar disc is too poor, then the disc artificially accretes rapidly due to the artificially enhanced effects of viscosity at low density in the SPH code.

We first examined the behaviour of initially highly inclined circumstellar discs that are not supplied with material from a CBD. A polar test particle in orbit around a primary star reaches an eccentricity of nearly unity during the first KL cycle, forcing the particle to become unbound or hit the central star. Similarly, initially highly inclined circumstellar discs around individual binary components can experience very strong KL oscillations. For an equal mass binary containing only a single circumstellar disc at high

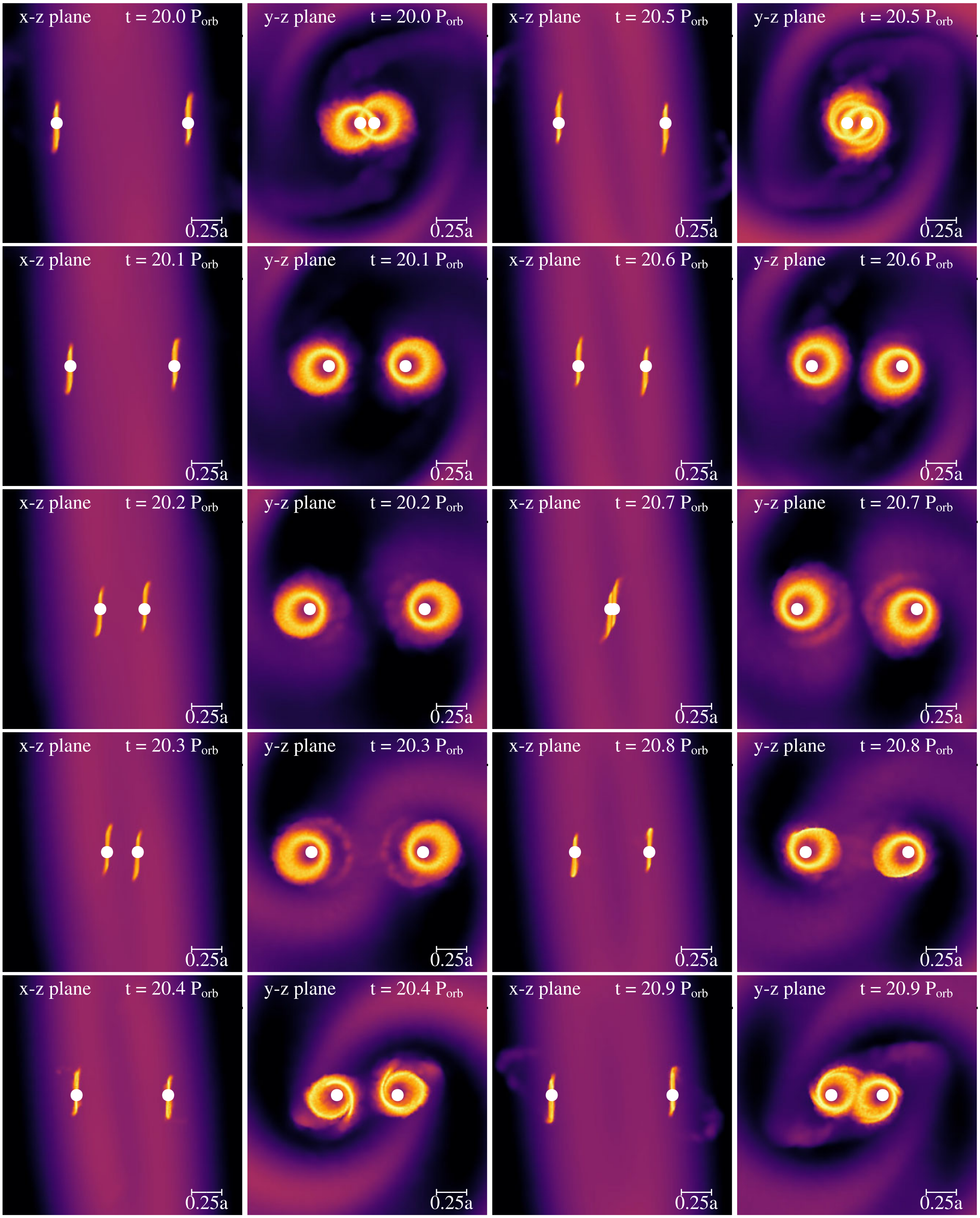

Figure 11. Zoomed-in snapshots of the disc surface density showing the flow of material from a polar CBD onto the nearly polar circumstellar discs. The white circles denote the eccentric orbit binary components with an initial binary separation of a. The colour denotes the gas density using a weighted density interpolation, which gives a mass-weighted line of sight average. The yellow regions are about three orders of magnitude larger than the purple. We view the orbit of the binary in the x–z and y–z planes. The snapshots show a period from 20 P$_{\rm orb}$ to 20.9 P$_{\rm orb}$ in increments of 0.1 P$_{\rm orb}$, where $P_{\rm orb}$ is time in binary orbital periods.

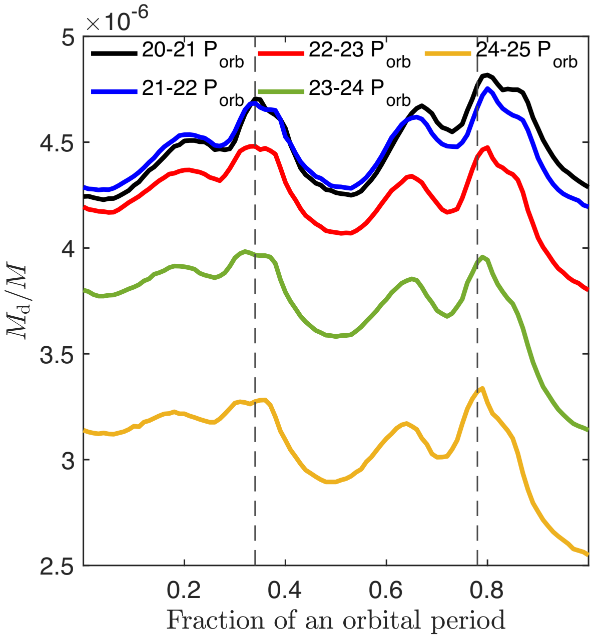

Figure 12. The CPD mass evolution during one binary orbital period, $\mathrm{P_{orb}}$, at times $20-21\,\mathrm{P_{orb}}$ (blue), $21-22\,\mathrm{P_{orb}}$ (red), $22-23\,\mathrm{P_{orb}}$ (yellow), $23-24\,\mathrm{P_{orb}}$ (purple), and $24-25\,\mathrm{P_{orb}}$ (green). The mass of the disc decreases every $0.5\,\mathrm{P_{orb}}$. The vertical-dashed lines denote the times when the binary is aligned with the CBD plane during $20-21\,\mathrm{P_{orb}}$. An increased flow of material onto the circumstellar discs occurs when the binary is aligned with the CBD plane.

inclination between 70° and 100°, the disc undergoes only a single KL oscillation before losing nearly all its mass for our given sink size. Some of the disc mass is transferred to the companion star to form a low inclination disc that does not undergo KL oscillations. These results suggests that such high inclinations of discs are short-lived due to enhanced dissipation from shocks that leads to tilt evolution on short time-scales. In contrast, discs that are highly inclined but are not subject to KL oscillations would undergo much slower evolution. In particular, a polar disc would not precess (see e.g. equation (7)) and therefore not warp. The disc would then not be subject to torques that act to change its inclination.

In this work, and from Smallwood et al. (2021b), we showed that the continuous accretion of material from the CBD allows the effects of KL oscillations on circumstellar discs to be much longer-lived. In this process, the circumbinary material is continuously delivered with a high inclination to the lower inclination circumstellar discs. We found that the simulation resolution is important for modelling the longevity of the KL oscillations. We find longer lived KL oscillations that show signs of mild weakening in time, possibly due to the resolution (e.g. Fig. 6). The balance between the accretion time-scale and the KL time-scale determines whether the oscillations are sustained or damp in time. If the circumstellar disc material were to accrete on a much shorter time-scale than the KL oscillation period, we would not expect the KL oscillations to operate. We found that with increasing resolution, the accretion time-scale becomes comparable to the KL time-scale, favouring sustained KL oscillations.

Planet formation is thought to still occur in non-zero eccentricity discs (Silsbee & Rafikov 2021). In the case of *S*-type planets (planets orbiting one of the stellar companions in a binary), gravitational perturbations from an eccentric orbit stellar companion and an eccentric disc increase planetesimal eccentricities, leading to collisional fragmentation, rather than growth, of planetesimals. However, Rafikov & Silsbee (2015) analysed the planetesimal motion in eccentric protoplanetary discs when the planetesimals were affected by gas drag and disc gravity. They found that the planetesimals could withstand collisional fragmentation and erosion, thereby providing a pathway to forming planetary cores by coagulation in a binary. It is not clear how those results carry over to the case of highly eccentric discs undergoing KL oscillations. However, the formation of nearly polar circumstellar discs from this work may give rise to the formation of nearly polar planets that become Kozai-unstable. Planet formation in a polar circumstellar disc requires the disc to last for a sufficiently long time. We speculate that this is possible provided that the disc is continuously accreting material in a polar configuration.

Observations of misaligned planetary systems show a preference for nearly polar orbits with true obliquities ψ in the range $\psi = 80^\circ - 125^\circ$ (Albrecht et al. 2021; Dawson & Albrecht 2021). For example, two observed ultra-short-period hot Jupiters in polar orbits around an A-type star are Kelt-9b (Ahlers et al. 2020a) and MASCARA-4b (Ahlers et al. 2020b). The majority of planets studied by Albrecht et al. (2021) were hot Jupiters, since the measurements for these types of planets are more precise. However, a few warm-Neptunes with polar orbits were observed, including HAT-P-11b (Sanchis-Ojeda & Winn 2011), GJ 436b (Bourrier et al. 2018, 2022), HD 3167c (Dalal et al. 2019; Bourrier et al. 2021), and WASP-107b (Dai & Winn 2017; Rubenzahl et al. 2021). A more recent warm Neptune, GJ 3470b, is also observed to be on a polar orbit (Stefànsson et al. 2022).

ACKNOWLEDGEMENTS

We thank the anonymous reviewer for helpful suggestions that positively impacted the work. We thank Daniel Price for providing the PHANTOM code for SPH simulations and acknowledge the use of SPLASH (Price 2007) for the rendering of the figures. Computer support was provided by UNLV's National Supercomputing Center. We acknowledge support from NASA XRP grants 80NSSC19K0443 and 80NSSC21K0395. This research was supported in part by the National Science Foundation under Grant Number NSF PHY-1748958. SHL thanks the Simons Foundation for support during a visit to the Flatiron Institute.

DATA AVAILABILITY

The data supporting the plots within this article are available on reasonable request to the corresponding author. A public version of the PHANTOM, SPLASH, and MERCURY codes are available at https://github.com/danieljprice/phantom, http://users.monash.edu.au/~dprice/splash/download.html, and https://github.com/4xxi/mercury, respectively.

REFERENCES

Ahlers J. P., et al., 2020a, AJ, 160, 4
Ahlers J. P., et al., 2020b, ApJ, 888, L63
Albrecht S. H., Marcussen M. L., Winn J. N., Dawson R. I., Knudstrup E., 2021, ApJ, 916, L1
Alves F. O., Caselli P., Girart J. M., Segura-Cox D., Franco G. A. P., Schmiedeke A., Zhao B., 2019, Science, 366, 90
Aly H., Lodato G., 2020, MNRAS, 492, 3306
Aly H., Dehnen W., Nixon C., King A., 2015, MNRAS, 449, 65
Antonini F., Perets H. B., 2012, ApJ, 757, L27
Armitage P. J., Natarajan P., 2005, ApJ, 634, L921
Artymowicz P., 1992, PASP, 104, 769

Artymowicz P., Lubow S. H., 1994, ApJ, 421, L651
Artymowicz P., Lubow S. H., 1996, ApJ, 467, L77
Artymowicz P., Clarke C. J., Lubow S. H., Pringle J. E., 1991, ApJ, 370, L35
Bate M. R., Bonnell I. A., Price N. M., 1995, MNRAS, 277, 362
Bi J., et al., 2020, ApJ, 895, L18
Blaes O., Lee M. H., Socrates A., 2002, ApJ, 578, L775
Bourrier V., et al., 2018, Nature, 553, 477
Bourrier V., et al., 2021, A&A, 654, 152
Bourrier V., et al., 2022, A&A, 663, 160
Brinch C., Jørgensen J. K., Hogerheijde M. R., Nelson R. P., Gressel O., 2016, ApJ, 830, L16
Chambers J. E., 1999, MNRAS, 304, 793
Chen X., Sesana A., Madau P., Liu F. K., 2011, ApJ, 729, L13
Chen C., Franchini A., Lubow S. H., Martin R. G., 2019, MNRAS, 490, 5634
Chiang E. I., Murray-Clay R. A., 2004, ApJ, 607, L913
Cuadra J., Armitage P. J., Alexander R. D., Begelman M. C., 2009, MNRAS, 393, 1423
Cuello N., Giuppone C. A., 2019, A&A, 628, 119
D'Angelo G., Lissauer J. J., 2018, Formation of Giant Planets. p. 140
D'Orazio D. J., Haiman Z., MacFadyen A., 2013, MNRAS, 436, 2997
Dai F., Winn J. N., 2017, AJ, 153, 205
Dalal S., Hébrard G., Lecavelier des Étangs A., Petit A. C., Bourrier V., Laskar J., König P. C., Correia A. C. M., 2019, A&A, 631, 28
Dawson R. I., Albrecht S. H., 2021, preprint (arXiv:2108.09325)
Deacon N. R., et al., 2016, MNRAS, 455, 4212
Doğan S., Nixon C., King A., Price D. J., 2015, MNRAS, 449, 1251
Duchêne G., Kraus A., 2013, ARA&A, 51, 269
Duquennoy A., Mayor M., 1991, A&A, 248, 485
Eggleton P. P., Kiseleva-Eggleton L., 2001, ApJ, 562, L1012
Fabrycky D., Tremaine S., 2007, ApJ, 669, L1298
Facchini S., Lodato G., Price D. J., 2013, MNRAS, 433, 2142
Facchini S., Juhász A., Lodato G., 2018, MNRAS, 473, 4459
Farris B. D., Duffell P., MacFadyen A. I., Haiman Z., 2014, ApJ, 783, L134
Ford E. B., Kozinsky B., Rasio F. A., 2000, ApJ, 535, L385
Foucart F., Lai D., 2014, MNRAS, 445, 1731
Fragione G., Grishin E., Leigh N. W. C., Perets H. B., Perna R., 2019a, MNRAS, 488, 47
Fragione G., Leigh N. W. C., Perna R., 2019b, MNRAS, 488, 2825
Franchini A., Martin R. G., Lubow S. H., 2019a, MNRAS, 485, 315
Franchini A., Lubow S. H., Martin R. G., 2019b, ApJ, 880, L18
Franchini A., Martin R. G., Lubow S. H., 2020, MNRAS, 491, 5351
Fu W., Lubow S. H., Martin R. G., 2015a, ApJ, 807, L75
Fu W., Lubow S. H., Martin R. G., 2015b, ApJ, 813, L105
Fu W., Lubow S. H., Martin R. G., 2017, ApJ, 835, L29
Ghez A. M., Neugebauer G., Matthews K., 1993, AJ, 106, 2005
Goldreich P., Tremaine S., 1980, ApJ, 241, L425
Günther R., Kley W., 2002, A&A, 387, 550
Hamers A. S.,Bar-Or B., Petrovich C., Antonini F. , 2018, ApJ, 865, L2
Hatzes A. P., Cochran W. D., Endl M., McArthur B., Paulson D. B., Walker G. A. H., Campbell B., Yang S., 2003, ApJ, 599, L1383
Hirsh K., Price D. J., Gonzalez J.-F., Ubeira-Gabellini M. G., Ragusa E., 2020, MNRAS, 498, 2936
Hoang B.-M., Naoz S., Kocsis B., Rasio F. A., Dosopoulou F., 2018, ApJ, 856, L140
Holman M., Touma J., Tremaine S., 1997, Nature, 386, 254
Horch E. P., Howell S. B., Everett M. E., Ciardi D. R., 2014, ApJ, 795, L60
Ichikawa T., Kido M., Takaishi D., Shimajiri Y., Tsukamoto Y., Takakuwa S., 2021, ApJ, 919, 55
Innanen K. A., Zheng J. Q., Mikkola S., Valtonen M. J., 1997, AJ, 113, 1915
Jang-Condell H., 2015, ApJ, 799, L147
Kennedy G. M., et al., 2012, MNRAS, 421, 2264
Kennedy G. M., et al., 2019, Nature Astron., 3, 230
Kiseleva L. G., Eggleton P. P., Mikkola S., 1998, MNRAS, 300, 292
Kozai Y., 1962, AJ, 67, 591
Kraus S., et al., 2020, Science, 369, 1233
Kushnir D., Katz B., Dong S., Livne E., Fernández R., 2013, ApJ, 778, L37
Larwood J. D., Nelson R. P., Papaloizou J. C. B., Terquem C., 1996, MNRAS, 282, 597
Li G., Naoz S., Holman M., Loeb A., 2014, ApJ, 791, L86
Lidov M. L., 1962, Planet. Space Sci., 9, 719
Lithwick Y., Naoz S., 2011, ApJ, 742, L94
Liu B., Muñoz D. J., Lai D., 2015, MNRAS, 447, 747
Lodato G., Price D. J., 2010, MNRAS, 405, 1212
Lodato G., Pringle J. E., 2007, MNRAS, 381, 1287
Lubow S. H., 2021, MNRAS, 507, 367
Lubow S. H., Martin R. G., 2018, MNRAS, 473, 3733
Lubow S. H., Martin R. G., Nixon C., 2015, ApJ, 800, L96
Lynden-Bell D., Pringle J. E., 1974, MNRAS, 168, 603
Marino S., Perez S., Casassus S., 2015, ApJ, 798, L44
Martin R. G., Franchini A., 2019, MNRAS, 489, 1797
Martin R. G., Lubow S. H., 2017, ApJ, 835, L28
Martin R. G., Lubow S. H., 2018, MNRAS, 479, 1297
Martin R. G., Lubow S. H., 2019, MNRAS, 490, 1332
Martin R. G., Nixon C., Armitage P. J., Lubow S. H., Price D. J., 2014a, ApJ, 790, L34
Martin R. G., Nixon C., Lubow S. H., Armitage P. J., Price D. J., Doğan S., King A., 2014b, ApJ, 792, L33
Miranda R., Lai D., 2015, MNRAS, 452, 2396
Muñoz D. J., Miranda R., Lai D., 2019, ApJ, 871, L84
Nagasawa M., Ida S., Bessho T., 2008, ApJ, 678, L498
Naoz S., Farr W. M., Lithwick Y., Rasio F. A., Teyssandier J., 2011, Nature, 473, 187
Naoz S., Farr W. M., Lithwick Y., Rasio F. A., Teyssandier J., 2013a, MNRAS, 431, 2155
Naoz S., Kocsis B., Loeb A., Yunes N., 2013b, ApJ, 773, L187
Nesvorný D., Alvarellos J. L. A., Dones L., Levison H. F., 2003, AJ, 126, 398
Nixon C. J., 2012, MNRAS, 423, 2597
Nixon C. J., King A. R., 2012, MNRAS, 421, 1201
Nixon C., Lubow S. H., 2015, MNRAS, 448, 3472
Nixon C., King A., Price D., 2013, MNRAS, 434, 1946
Owen J. E., Lai D., 2017, MNRAS, 469, 2834
Papaloizou J., Pringle J. E., 1977, MNRAS, 181, 441
Perets H. B., Fabrycky D. C., 2009, ApJ, 697, L1048
Pichardo B., Sparke L. S., Aguilar L. A., 2005, MNRAS, 359, 521
Poblete P. P., Cuello N., Cuadra J., 2019, MNRAS, 489, 2204
Poon M., Zanazzi J. J., Zhu W., 2021, MNRAS, 503, 1599
Price D. J., 2007, PASA, 24, 159
Price D. J., et al., 2018a, PASA, 35, e031
Price D. J., et al., 2018b, MNRAS, 477, 1270
Pringle J. E., 1991, MNRAS, 248, 754
Rafikov R. R., Silsbee K., 2015, ApJ, 798, L69
Raghavan D., et al., 2010, ApJS, 190, 1
Ragusa E., Alexander R., Calcino J., Hirsh K., Price D. J., 2020, MNRAS, 499, 3362
Ragusa E., et al., 2021, MNRAS, 507, 1157
Roedig C., Dotti M., Sesana A., Cuadra J., Colpi M., 2011, MNRAS, 415, 3033
Rubenzahl R. A., et al., 2021, AJ, 161, 119
Sanchis-Ojeda R., Winn J. N., 2011, ApJ, 743, L61
Shakura N. I., Sunyaev R. A., 1973, A&A, 24, 337
Shi J.-M., Krolik J. H., Lubow S. H., Hawley J. F., 2012, ApJ, 749, L118
Silsbee K., Rafikov R. R., 2021, A&A, 652, 104
Smallwood J. L., Lubow S. H., Franchini A., Martin R. G., 2019, MNRAS, 486, 2919
Smallwood J. L., Franchini A., Chen C., Becerril E., Lubow S. H., Yang C.-C., Martin R. G., 2020, MNRAS, 494, 487
Smallwood J. L., Nealon R., Chen C., Martin R. G., Bi J., Dong R., Pinte C., 2021a, MNRAS, 508, 392
Smallwood J. L., Martin R. G., Lubow S. H., 2021b, ApJ, 907, L14
Stefànsson G., et al., 2022, ApJ, 931, L15
Takeda G., Rasio F. A., 2005, ApJ, 627, L1001
Teyssandier J., Terquem C., Papaloizou J. C. B., 2013, MNRAS, 428, 658

Thompson T. A., 2011, ApJ, 741, L82
Tokovinin A., 2014a, AJ, 147, 86
Tokovinin A., 2014b, AJ, 147, 87
Tokovinin A., Kiyaeva O., 2016, MNRAS, 456, 2070
Wu Y., Murray N., 2003, ApJ, 589, L605
Zahn J.-P., 1977, A&A, 57, 383
Zanazzi J. J., Lai D., 2018, MNRAS, 473, 603
Ziegler C., et al., 2018, AJ, 155, 161
Zrake J., Tiede C., MacFadyen A., Haiman Z., 2021, ApJ, 909, L13

This paper has been typeset from a TEX/LATEX file prepared by the author.